Supplemental Material for "Paramagnons and high-temperature superconductivity in mercury-based cuprates"

Lichen Wang[1,2], Guanhong He[1], Zichen Yang[2], Mirian Garcia-Fernandez[3], Abhishek Nag[3], Kejin Zhou[3], Matteo Minola[2], Matthieu Le Tacon[4], Bernhard Keimer[2], Yingying Peng[1,5], Yuan Li[1,5]

[1]*International Center for Quantum Materials, School of Physics, Peking University, Beijing 100871, China*

[2]*Max Planck Institute for Solid State Research, Stuttgart 70569, Germany*

[3]*Diamond Light Source, Harwell Science & Innovation Campus, Didcot, Oxfordshire OX11 0DE, United Kingdom*

[4]*Institute for Quantum Materials and Technologies, Karlsruhe Institute of Technology, Karlsruhe 76133, Germany*

[5]*Collaborative Innovation Center of Quantum Matter, Beijing 100871, China*

S1. Sample preparation and characterization

The Hg1201 and Hg1212 single crystals used in this study were grown with a self-flux method [1,2]. Photos of the crystals are displayed in Fig. S1a. The crystals were post-growth annealed over extended periods of time in air at 480 °C, in order to reach homogeneous doping as indicated by their sharp transitions at T_c (Fig. S1b) determined from magnetometry (Quantum Design MPMS VSM). The resultant doping levels are estimated [3] to be $p \sim 0.11$ for Hg1201 and 0.12 for Hg1212 based on their T_c values of 80 K and 107 K, respectively, using a simplified relation: $T_c = T_{c,max}*(1 - 82.6*(p - 0.16)^2)$. The good crystallinity is demonstrated by single-crystal *x*-ray diffraction (Rigaku MiniFlex 600) and *x*-ray Laue diffraction (Photonic Science, Fig. S1a&c). For both the RIXS and Raman measurements, the crystals were freshly polished along their *ab* plane with 0.05 μm-grade 3M lapping films before being loaded into vacuum.

S2. RIXS experiment

The RIXS experiments were performed at beamline I21 of Diamond Light Source, Didcot, United Kingdom. The incident *x*-ray energy was tuned to the L_3 absorption edge of Cu^{2+} at about 931.5 eV,

and was calibrated frequently during the experiments by performing *x*-ray absorption spectroscopy measurements in the total fluorescence yield mode. The beam size on sample with full flux was 40(H)*2.5(V) μm^2. The total instrumental bandwidth (energy resolution) at the Cu L_3 absorption edge was about 37 meV, determined as the full-width at half-maximum (FWHM) of the diffuse scattering peak from a carbon tape mounted at the sample position. With the exception of some data in Fig. S12, all RIXS spectra were obtained using π-polarized incident *x*-rays for maximal sensitivity to single spin-flip excitations. The polarization state of the scattered phonons was not analyzed. All RIXS spectra were collected at a temperature of about 13 K. The raw data are displayed in Fig. S2, with momentum coverage along two high-symmetry directions of the first magnetic Brillouin zone. The lattice parameters we used for calculating the scattering geometry were $a = b = 3.840$ Å, $c = 9.435$ Å for Hg1201, and $a = b = 3.788$ Å, $c = 12.557$ Å for Hg1212.

S3. Raman scattering experiment

The Raman scattering experiments were performed in a confocal back-scattering geometry using a Horiba Jobin Yvon LabRAM HR Evolution spectrometer equipped with 600 lines/mm grating, a liquid-nitrogen-cooled CCD detector and a He-Ne laser with $\lambda = 632.8$ nm as the excitation line. During the measurements, the samples were kept in a liquid-helium flow cryostat (ARS) under an ultrahigh vacuum (~10^{-8} torr), and all data were obtained in the B_{1g} scattering geometry [4], with the incident and the scattered photons linearly polarized perpendicular to each other and along the diagonals of the CuO_2 plaquettes. The laser power on the sample was kept below 0.65 mW, thereby avoiding heating effects.

The Bose-factor corrected Raman spectra are displayed in Fig. S8a&b. The data have been corrected for the optical response of the measurement system, and normalized around 0.33 and 0.38 eV Raman shift for Hg1201 and Hg1212, respectively. Defect phonon peaks ranging from 450 cm^{-1} to 650 cm^{-1} [2] have been removed from the spectra to focus the attention on the electronic Raman scattering signal. Both the pair-breaking peak and the bi-paramagnon peak become most evident in the data taken at low temperatures after subtracting the 300 K spectrum as reference (Fig. S8c&d). However, the bi-paramagnon peak is already present as a broad hump at 300 K. Thus, in this way, the bi-paramagnon peak that we present in Fig. 3 should be regarded as the temperature-dependent part of the bi-paramagnon signals.

S4. Analysis of RIXS spectra

To facilitate a systematic analysis and comparison of the RIXS spectra, we first normalize the spectra

taken at different $\mathbf{Q}_{//}$ to the intensity of the *dd* excitations [5] (from 1 eV to 3.5 eV, based on data in Fig. S2). The normalized data acquired at different $\mathbf{Q}_{//}$ for Hg1201 and Hg1212 are then compared in Figs. S3-4.

We describe the RIXS intensities below 1 eV with a total of five spectral components: a resolution-limited elastic peak, a resolution-limited single-phonon peak, a weakly resolution-limited two-phonon peak, a paramagnon peak, and a weakly-energy-dependent background. The resolution-limited components are modelled by Gaussian peaks of fixed FWHM of 37 meV, and the weakly-resolution-limited component is described by convolving the Gaussian peak with a Lorentzian peak of smaller FWHM than the Gaussian peak. The background component is modelled by a Lorentzian peak centered at the energy of the *dd* excitations (the background is just the tail of this peak). The paramagnon component is described by a generic damped harmonic oscillator $L(\omega)$ convolved with the Gaussian resolution function,

$$L(\omega) = \frac{\gamma\omega}{\left(\omega^2-\omega_0^2\right)^2+4\gamma^2\omega^2}$$

where ω_0 is the undamped frequency and γ is damping. When $\gamma < \omega_0$, this function can be identically reproduced as an anti-symmetrized Lorentzian peak for $\omega > 0$,

$$L(\omega) = \frac{1}{4\omega_p}\left(\frac{\gamma}{\left(\omega-\omega_p\right)^2+\gamma^2}-\frac{\gamma}{\left(\omega+\omega_p\right)^2+\gamma^2}\right)$$

where the propagation frequency $\omega_p^2 = \omega_0^2 - \gamma^2$. Therefore, ω_p lacks definition when $\gamma > \omega_0$, as is the case for $\mathbf{Q}_{//}$ along (H, H) due to the overdamped nature of the paramagnons (Fig. S5 and Table S1).

The fitting procedure first requires to fix the individual spectrum's zero energy according to the center position of the elastic peak, which in subsequent iterations of the fitting is set to zero. The model parameters are then determined by the least-square method, where most parameters are considered momentum-dependent and free to vary, except for certain constrains on the inessential parameters concerning the two-phonon peak and the background. Specifically, the two-phonon peak energy is assumed to be independent of $\mathbf{Q}_{//}$ because it is found to be weakly dispersive. The peak position of the Lorentzian-tail-like background was fixed to the energy of the *dd* excitation [6]. The resultant best-fit parameters concerning the paramagnon component, and the associated comparison

between Hg1201 and Hg1212, are presented in Figs. S5-6 and Tables S1-2. We note that while our RIXS data for Hg1201 are consistent with those in a recent report on Hg1201 [7] wherever a direct comparison can be made (Fig. S11), details of the analyses might be different. By using the same method to analyze both Hg1201 and Hg1212, we are able to minimize systematic errors concerning the quantitative comparison between the two compounds.

Because our RIXS data are of very high statistical accuracy and energy-sampling density, the accuracy of model-parameter estimation, especially on the parameters concerning the paramagnon signal, is not limited by the data quality but rather by the accuracy of the model. Therefore, given that the first step of our fitting involves a self-correction of the zero-energy reference point using the resolution-limited elastic peak, whenever the fitting uncertainty on the paramagnon energy parameters (ω_0 or ω_p, which in turn determines the maximal-intensity energy ω_{max}) is smaller than 19 meV, the half-width at half-maximum of the resolution function, we consider the uncertainty to be 19 meV. In addition, we have found that the background amplitude can affect the estimation of ω_{max}, ω_0, γ and ω_p, hence we estimate the size of their confidence range by manually fixing the background amplitude to its allowable maximum according to the data and observing how the fit results vary. In this way, we conclude that we have considerably larger uncertainty in the determination of ω_0 and γ along (H, H) than (H, 0) (Fig. S5), and also for ω_p at smaller H along (H, 0) (Fig. S6). This result is generally consistent with previous RIXS results for doped cuprates, *e.g.,* in Ref. [8]. The fitted value of ω_p exhibits a dip-like structure in its dispersion between H = 0.2 and 0.3 along (H, 0). As this momentum range corresponds to short-range charge correlations in the Hg-family of cuprates [7,9-11], as is also suggested by the elastic-peak intensity in our RIXS data (Fig. S12), the result is consistent with the notion that there is an interplay between the charge and magnetic correlations and the associated properties of their excitations [12].

S5. Extraction of *J* for different cuprates

In order to compare J among different cuprates, we consider a nearest-neighbor-coupled spin-1/2 Heisenberg model on a square lattice:

$$H = J \sum_{\langle i,j \rangle \in NN} \boldsymbol{S}_i \cdot \boldsymbol{S}_j$$

where J is the Heisenberg antiferromagnetic interaction between the nearest neighbors. In our case of doped Hg1201 and Hg1212, the paramagnon propagation energy ω_p lacks its definition along (H, H)

due to the overdamped nature of the RIXS signals. Thus, we only consider ω_p dispersion along (H, 0) for the extraction of J for other cuprates as well, in order to maintain the most consistent standard. The neglection of potential difference between different cuprates concerning the zone-boundary dispersion of the (para)magnons [13] might lead to slight relative underestimation of J in CCOC and LSCO compared to the others in Fig. 4, but this will not affect our conclusion. Using linear spin-wave theory, the dispersion of the paramagnon energy can be simply written as $\omega(H) = 2J\sqrt{1-(\cos(2\pi H)+1)^2/4}$, where H is the value in $\mathbf{Q}_{//}$ = (H, 0) in units of r.l.u.

As doping increases, the (para)magnon signal becomes broadened in energy, but the high-energy part of the spin excitations near the zone corner (0.5, 0) have been demonstrated to hardly change, both experimentally [8,14] and theoretically [15], compared to the parent compound. We therefore consider it physically reasonable to rely on reported values of ω_p, available for LSCO [16], CCOC [17], YBCO [18], Y124 [19], NBCO [13,19], Tl2201 [18], Bi2201 [8], Bi2212 [20,21], Bi2223 [20], for the extraction of J. For parent compounds, we use ω_p at all measured momenta along (H, 0). For doped cuprates, we only use ω_p at $\mathbf{Q}_{//} \geq$ (0.3, 0) where the influence of damping, manifested as the departure of ω_p from ω_{max}, is relatively small. Our fitting of the published data is presented in Fig. S9, and the extracted values of J are summarized in Table S4 with uncertainty estimated based on the fits. Alternatively, we have also attempted to compare T_c directly to the (para)magnon energies near the magnetic zone corner ($\omega_{p,max}$), which are summarized in Table S4 and plotted in Fig. S10.

S6. Structural properties of different cuprates

In Table S3, we summarize some key aspects of structural properties, along with their values of $T_{c,max}$ and most prominent disorder site (when doped). The associated structural data were originally reported in Refs. [22-39]. Materials with higher $T_{c,max}$ are generally observed to be those with larger Cu-O-Cu angle [38], lager Cu-O apical distance [38], weaker structure disorder [39], and larger hopping ranges [13,40].

Supplementary References:

[1] X. Zhao *et al*., *Adv. Mater*. **18**, 3243–3247 (2006).

[2] L. Wang *et al*., *Phys. Rev. Mater.* **2,** 123401 (2018).

[3] N. Barišić *et al*., *Phys. Rev. B* **78,** 054518 (2008).

[4] T. P. Devereaux, and R. Hackl, *Rev. Mod. Phys.* **79,** 175(2007).

[5] L. Braicovich *et al*., *Phys. Rev. B* **81,** 174533 (2010).

[6] M. Moretti Sala *et al*., *New J. Phys.* **13,** 043026 (2011).

[7] B. Yu *et al*., *Phys. Rev. X* **10,** 021059 (2020).

[8] Y. Peng *et al*., *Phys. Rev. B* **98,** 144507 (2018).

[9] W. Tabis *et al*., *Nature Commun.* **5,** 5875 (2014).

[10] B. Loret *et al*., *Nature Phys.* **15,** 771–775 (2019).

[11] L. Wang *et al., Phys. Rev. B* **101,** 220509(R) (2020).

[12] H. Miao *et al., Proc. Nat. Acad. Sci.* **114**, 12430 (2017).

[13] Y. Peng *et al*. *Nature Phys.* **13,** 1201–1206 (2017).

[14] M. P. M. Dean *et al*., *Phys. Rev. Lett.* **110,** 147001 (2013).

[15] C. Jia *et al*., *Nature Commun.* **5,** 3314 (2014).

[16] N. S. Headings *et al*., *Phys. Rev. Lett.* **105**, 247001 (2010).

[17] B. W. Lebert *et al*., *Phys. Rev. B* **95,** 155110 (2017).

[18] M. Le Tacon *et al*., *Phys. Rev. B* **88,** 020501 (2013).

[19] M. Le Tacon *et al*., *Nature Phys.* **7,** 725–730 (2011).

[20] M. P. M. Dean *et al*., *Phys. Rev. B* **90,** 220506 (2014).

[21] Y. Peng *et al*., *Phys. Rev. B* **92,** 064517 (2015).

[22] Q. Huang, *et al*., *Phys. Rev. B* **52,** 462 (1995).

[23] P. G. Radaelli *et al*., *Physica C* **216,** 29 (1993).

[24] J. L. Wagner *et al.*, *Phys. Rev. B* **51,** 15407 (1995).

[25] J. L. Wagner *et al*., *Physica C* **277,** 170 (1997).

[26] M. Subramanian *et al.*, *Nature* **332,** 420–422 (1988).

[27] D. C. Sinclair *et al*., *Physica C* **225,** 307 (1994).

[28] C. C. Torardi *et al*., *Phys. Rev. B* **38,** 225–231 (1988).

[29] R. E. Gladyshevskii, and R. Flükiger, *Acta Cryst. B* **52,** 38 (1996).

[30] V.F. Shamray *et al*., *Crystallogr. Rep.* **54,** 584 (2009).

[31] K. Takita *et al*., *J. Phys. Chem. Solids* **27,** L57 (1988).

[32] G. Calestani, and C. Rizzoli, *Nature* **328,** 606–607 (1987).

[33] P. Lightfoot *et al*., *Acta Cryst. C* **47,** 1143–1145 (1991).

[34] P. G. Radaelli *et al*., *Phys. Rev. B* **49,** 4163–4175 (1994).

[35] H. Shaked *et al*., *Phys. Rev. B* **48,** 12941–12950 (1993).

[36] D. N. Argyriou *et al*., *Phys. Rev. B* **51,** 8434–8437 (1995).

[37] A. A. Ivanov *et al*., *J. Supercond. Nov. Magn.* **31,** 663 (2018).

[38] J.D. Jorgensen, *Adv. in Supercond. XII. Springer, Tokyo.* (2000).

[39] H. Eisaki *et al*., *Phys. Rev. B* **69,** 064512 (2004).

[40] E. Pavarini *et al*., *Phys. Rev. Lett.* **87,** 047003 (2001).

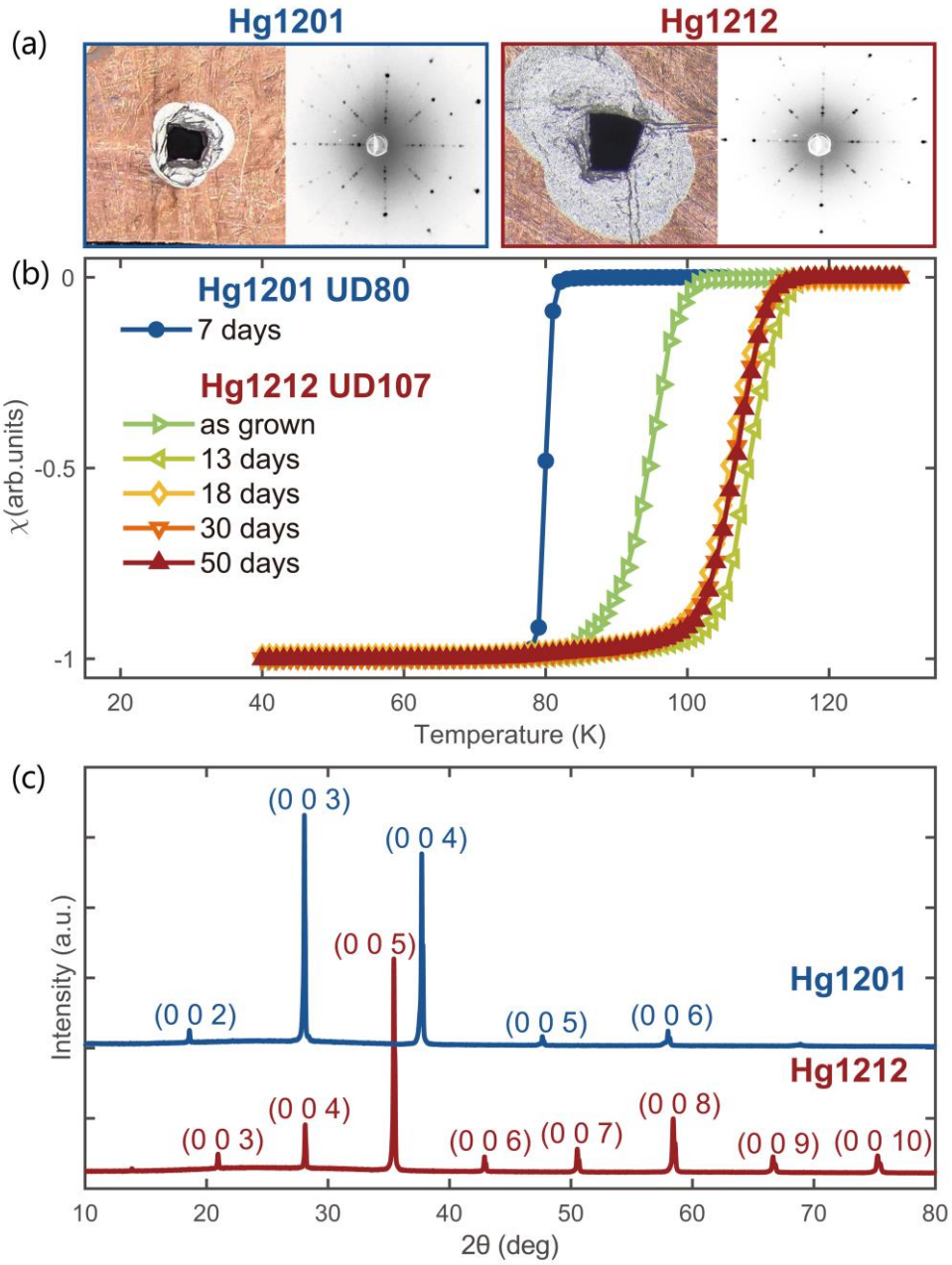

Figure S1. Hg1201 and Hg1212 crystals used in this study. (a) Photos of our Hg1201 and Hg1212 crystals mounted on a copper sample holder, before the RIXS experiments. X-ray Laue images taken on natural surfaces of Hg1201 and Hg1212 single crystals are displayed together. (b) Magnetic susceptibility measurements of our crystals after annealing in air at 480 °C for the indicated amounts of time. The measurements were performed upon warming the crystals with a magnetic field of 5 Oe applied along the *c* axis, after cooling the crystals in zero field. T_c is determined from the midpoint of the transitions to be 80 K and 107 K for Hg1201 and Hg1212, respectively, at the end of the annealing. (c) X-ray diffraction data taken on single crystals of Hg1201 and Hg1212, with the momentum transfer along the *c* axis. The *c*-axis lattice constants are determined to be 9.53 Å and 12.63 Å at room temperature, respectively.

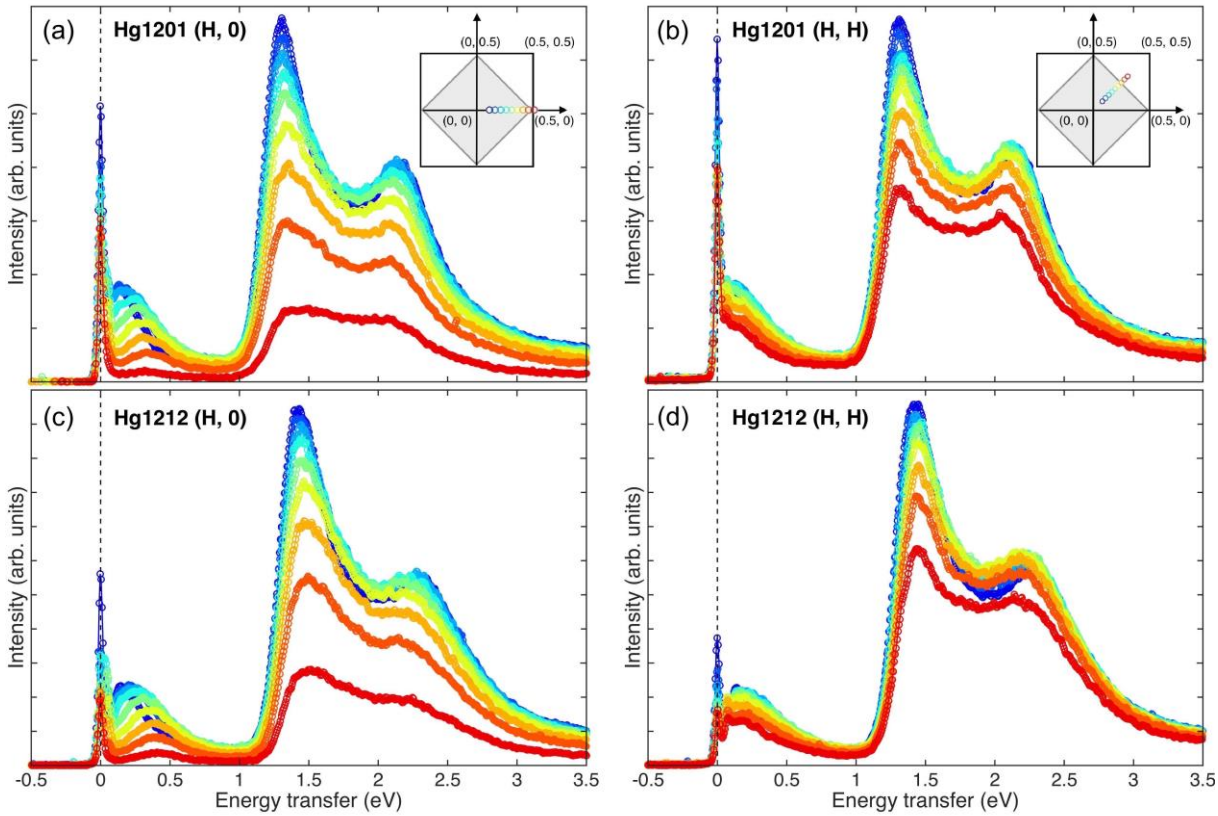

Figure S2. Raw RIXS spectra including *dd* excitations. (a)-(b) Raw spectra measured at $\mathbf{Q}_{//}$ = (*H*, 0) and (*H*, *H*) for Hg1201, respectively. (c)-(d) Raw spectra for Hg1212. Insets indicate the in-plane momentum trajectories, color-coded with the data points; grey area is the first magnetic Brillouin zone.

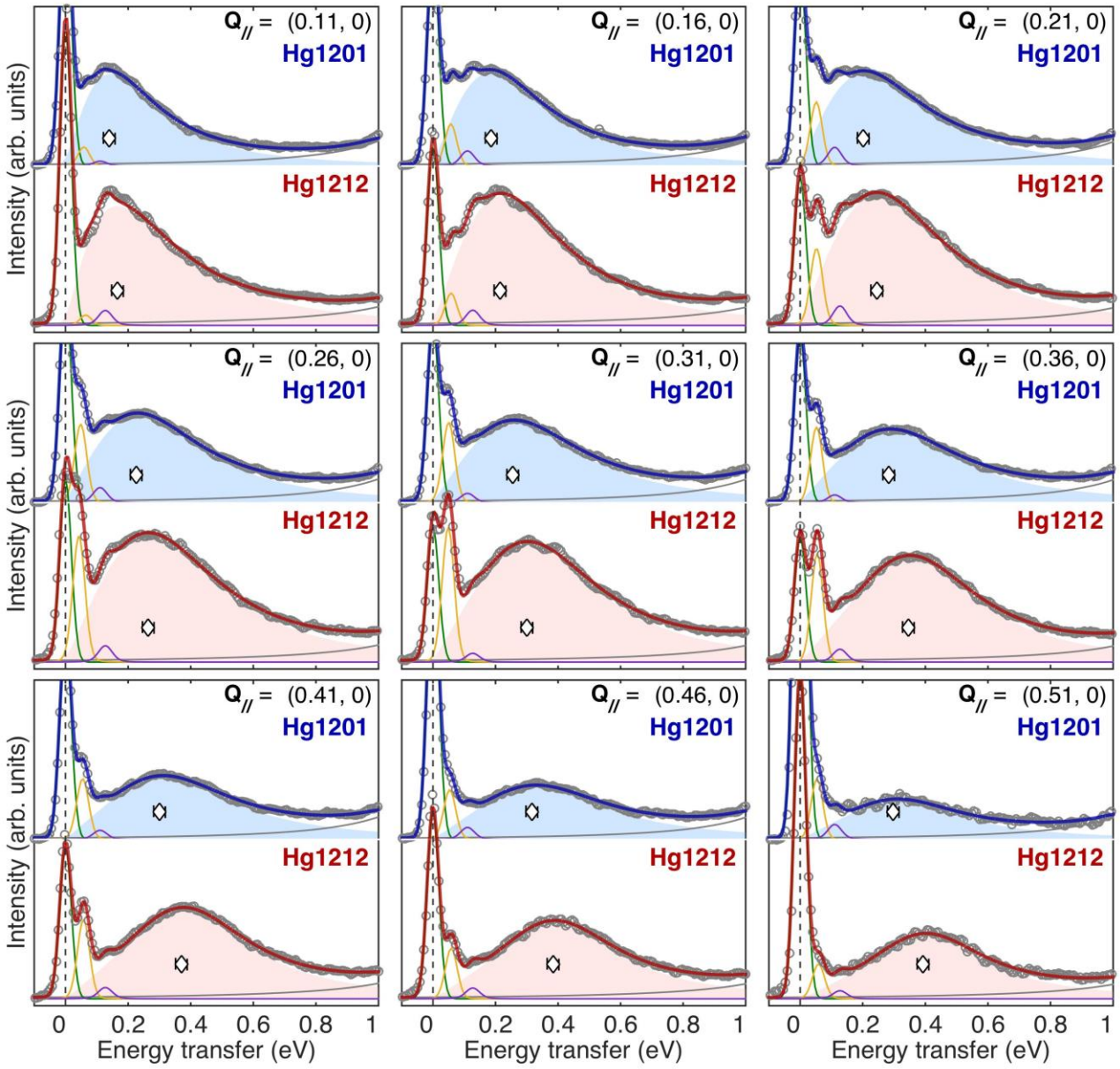

Figure S3. Q-by-Q comparison and decomposition of RIXS spectra along (*H*, 0). Empty circles are measurement data points. The spectra are decomposed into a sum of an elastic peak (green), a single-phonon peak (yellow), a two-phonon peak (magenta), a paramagnon peak (shaded area), and a weakly energy-dependent background (grey). Blue and red solid lines are the sum of all best-fit components for Hg1201 and Hg1212, respectively. Diamond symbols indicate the energy position of the paramagnon peak's maximum, error bar representing the uncertainty of the estimate (1 s.d.). Vertical dashed line marks the zero energy, which is set by the fit result of the elastic peak position. Summary of fitting parameters for the paramagnon component is presented in Table S1.

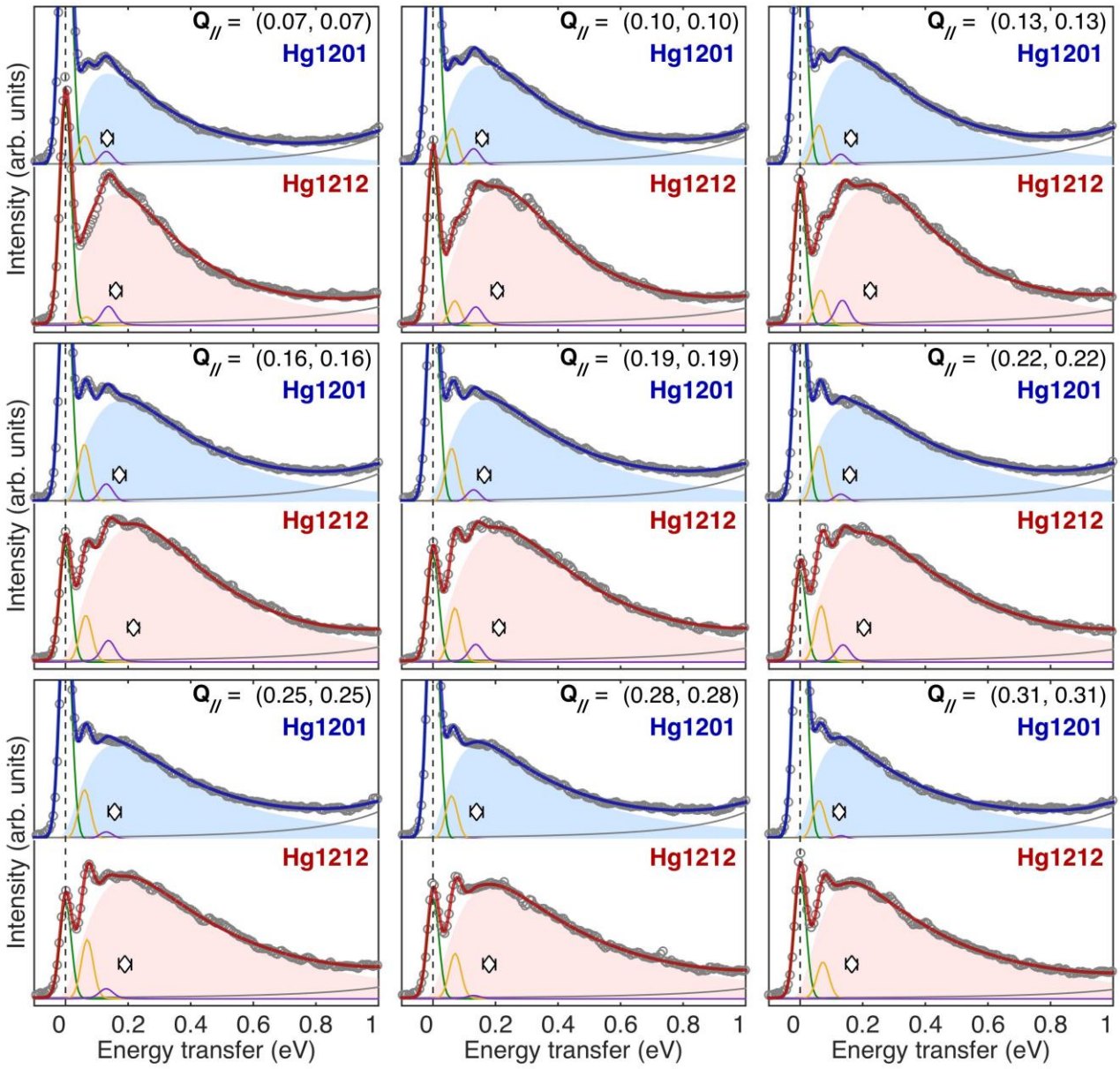

Figure S4. Q-by-Q comparison and decomposition of RIXS spectra along (*H*, *H*). See captions of Figure S3.

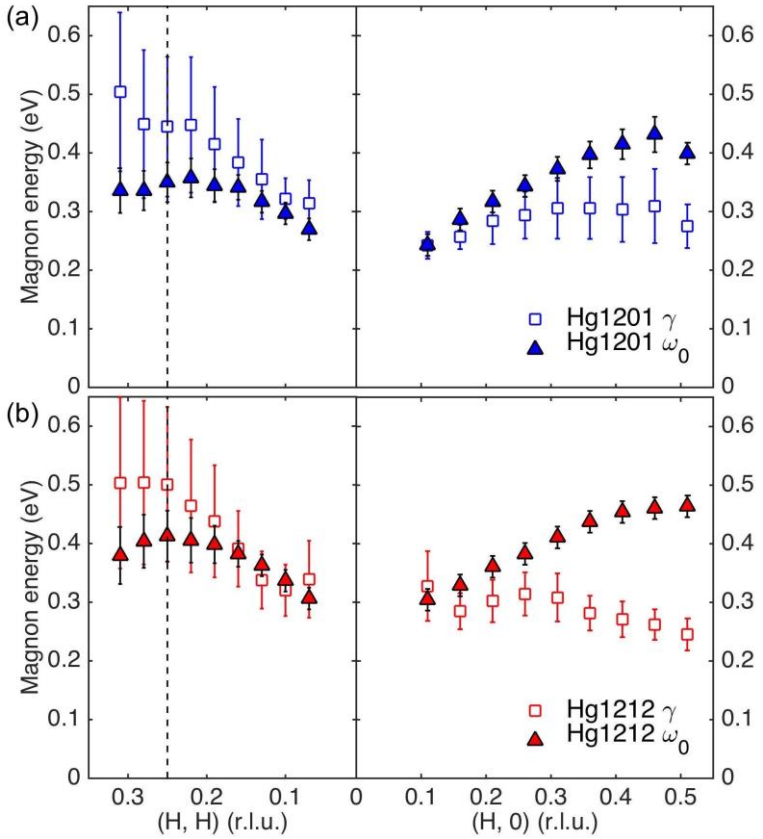

Figure S5. The undamped energy ω_0 and the damping γ for Hg1201 and Hg1212. Vertical dashed line indicates magnetic zone boundary along (*H*, *H*). Error bars indicate uncertainty of the fitting estimate (1 s.d.), see Supplemental Text for details.

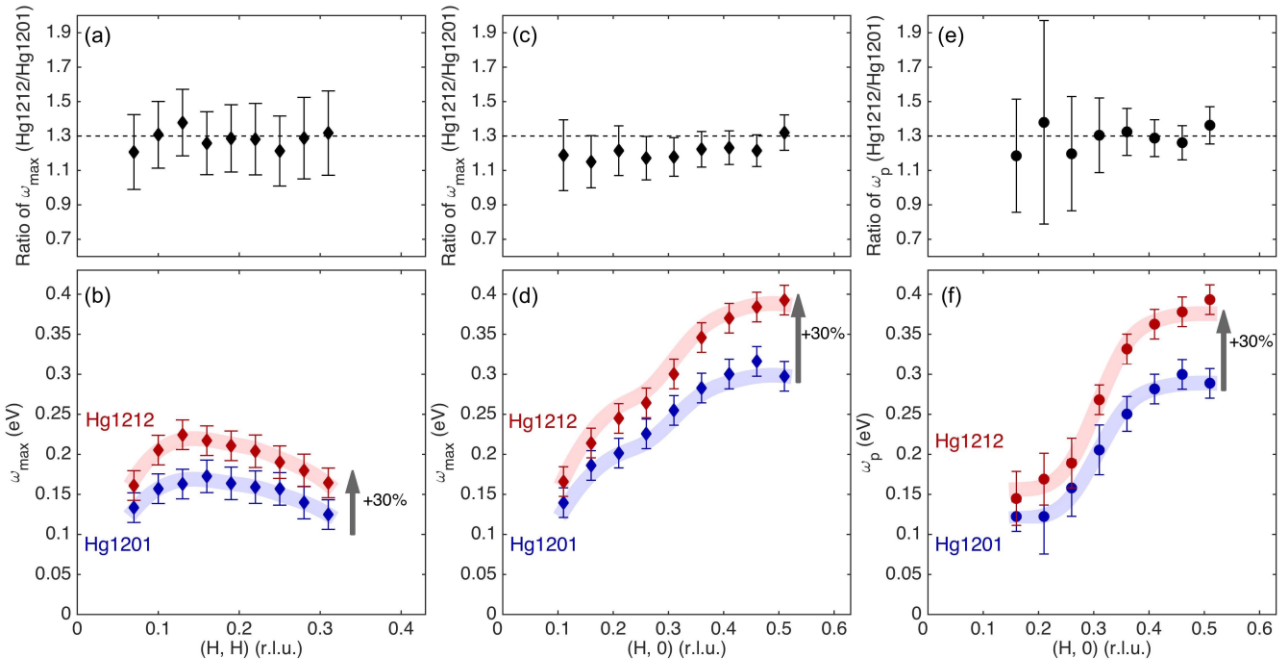

Figure S6. ω_{max}, ω_p and their ratios between Hg1201 and Hg1212. (a)-(b) The ratios of ω_{max} between Hg1201 and Hg1212 along $\mathbf{Q}_{//}$ = (H, H) and the estimated values of ω_{max}, respectively. The horizontal dashed line is a reference at 1.3, and the solid curves are guide to the eye with a 30% increase of ω_{max} from Hg1201 to Hg1212. (c)-(d) same as (a)-(b), but along (H, 0). (e)-(f) same as (a)-(b), but for ω_p along (H, 0). All the plotted values and uncertainties (error bars, 1 s.d.) are summarized in Table S2.

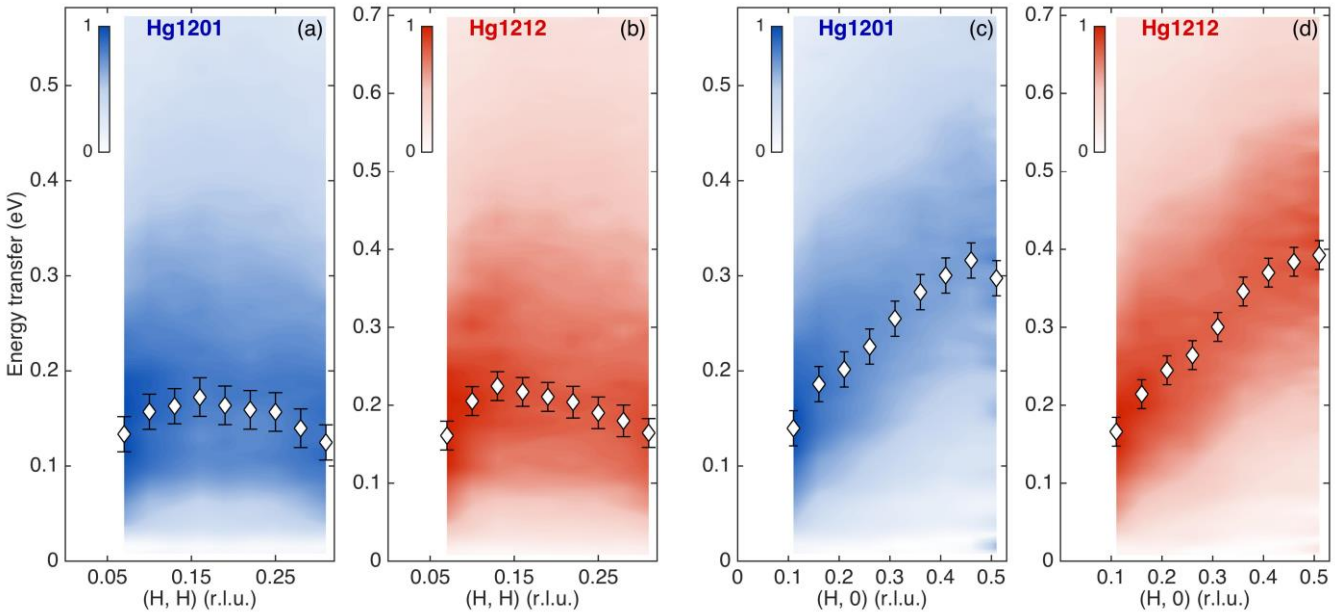

Figure S7. Alternative comparison of paramagnon energy scales. Same as Fig. S2, but with the Hg1212 panels (b) and (d) having an energy scale 122% that of the Hg1201 panels (a) and (c).

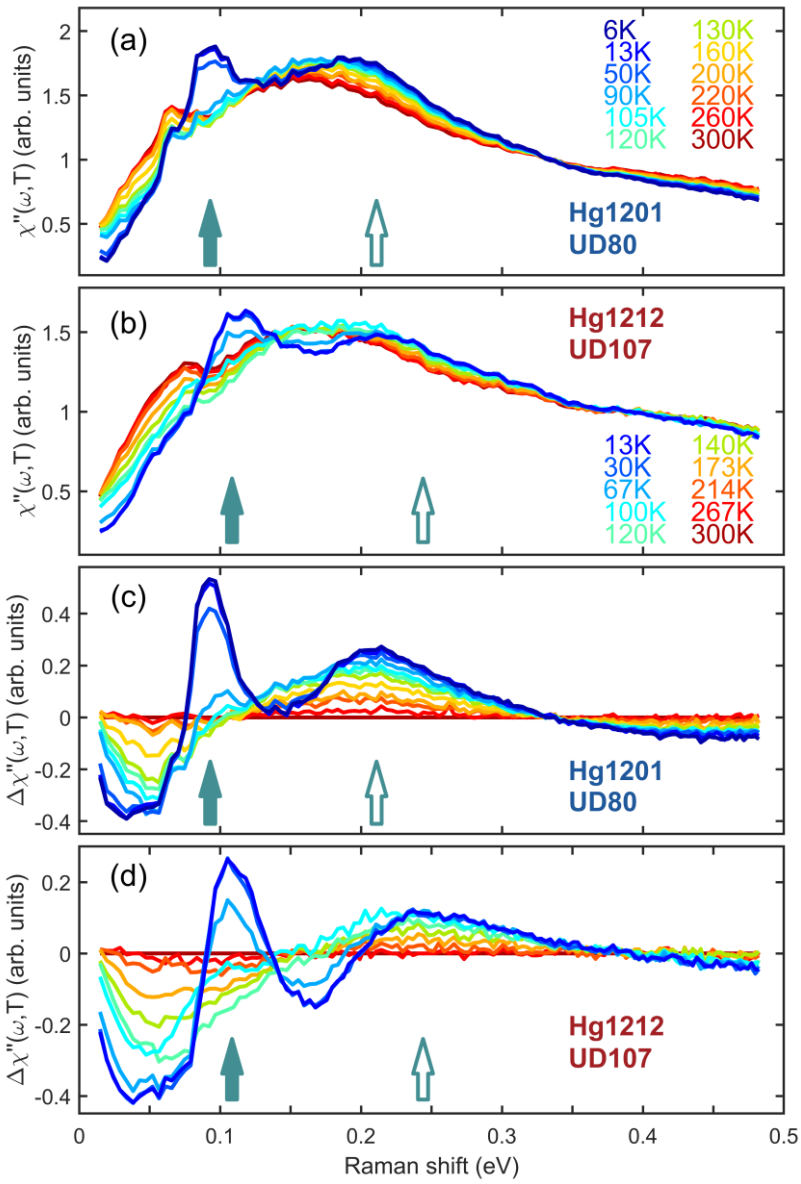

Figure S8. Full data set of electronic Raman scattering spectra. (a)-(b) Bose-factor-corrected B_{1g} spectra for Hg1201 and Hg1212, respectively. (c)-(d) Spectral change relative to 300 K. Solid and empty arrows indicate the energies of the pair-breaking peak and the bi-paramagnon peak at the lowest measured temperature, respectively.

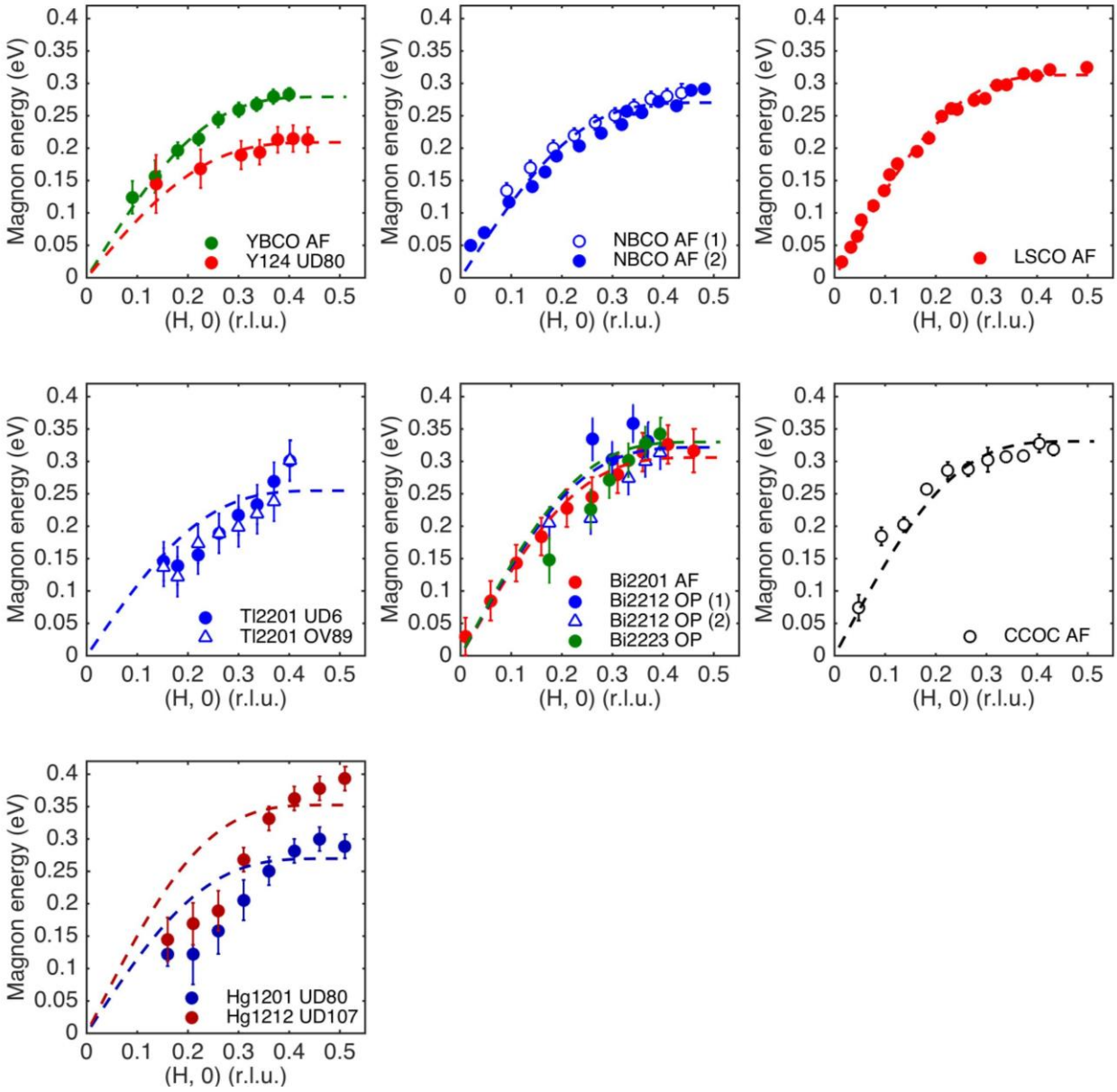

Figure S9. Extraction of J for different cuprates. We consider the propagation energy ω_p, which is the same as ω_0 and ω_{max} for antiferromagnetic (AF) parent compounds. Sources of data and the results of the fitting are summarized in Table S3. For doped cuprates, only data points at $H \geq 0.3$ are considered for the fits.

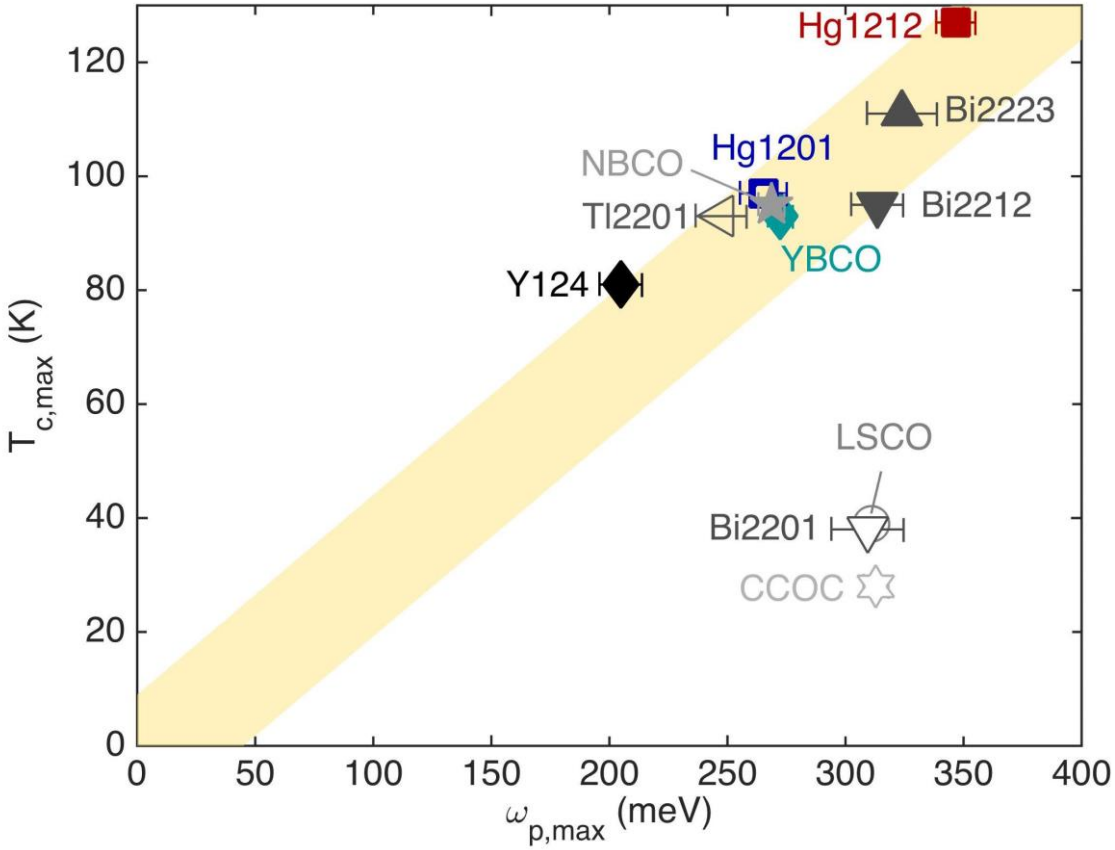

Figure S10. $T_{c,max}$ versus $\omega_{p,max}$ in different cuprates. $\omega_{p,max}$ is the averaged propagation frequency close to the zone corner ($\mathbf{Q}_{//}$ = (0.30, 0) and above). All values are determined from in Fig. S9 and listed in Table S4. Solid line is a guide to the eye.

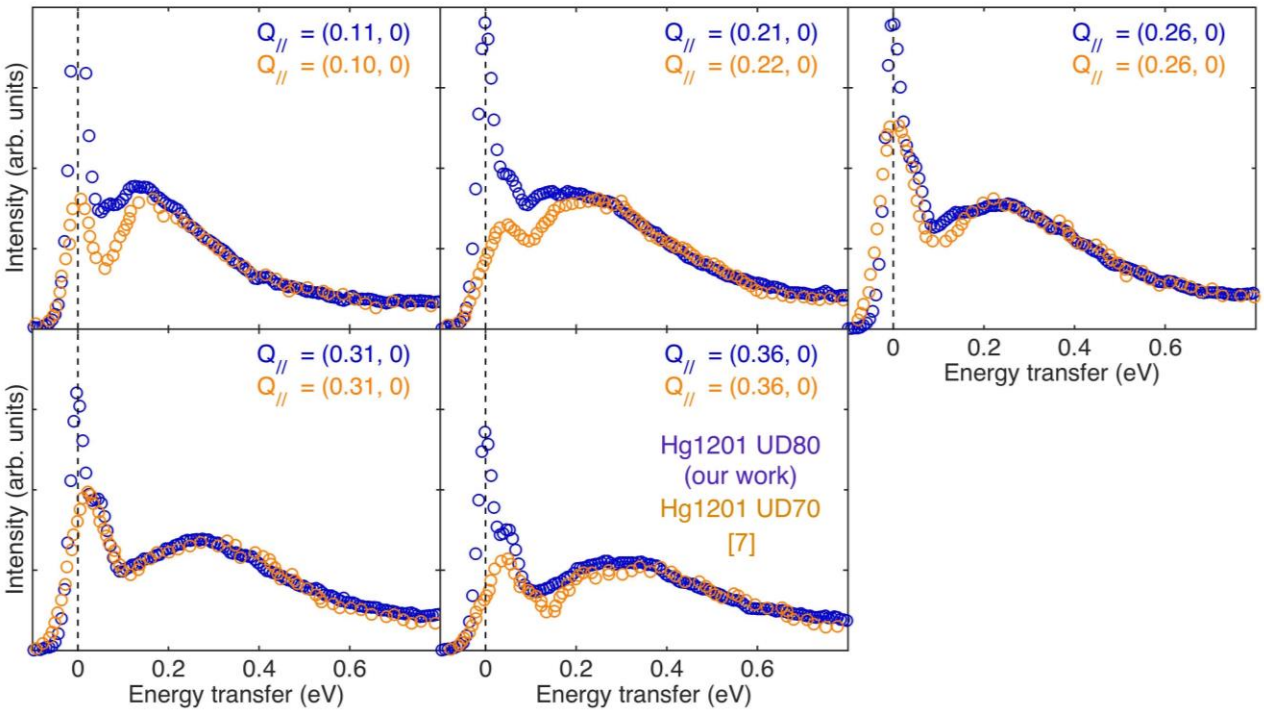

Figure S11. Comparison of our RIXS spectra for Hg1201 with published data. Blue circles are our data on Hg1201 UD80 taken with the π–polarized incident x-rays and an overall energy resolution of 37 meV. Orange circles are data digitalized from the supplemental materials for Ref. [7] taken on a crystal of somewhat lower doping (UD70), with π–polarized incident x-rays and 60 meV energy resolution. The two data sets are normalized by the intensity at around 0.8 eV. Despite the different manifestations of the elastic and single-phonon intensities which are partly affected by the difference in the energy resolution, the broad paramagnon peaks are highly consistent between the two data sets.

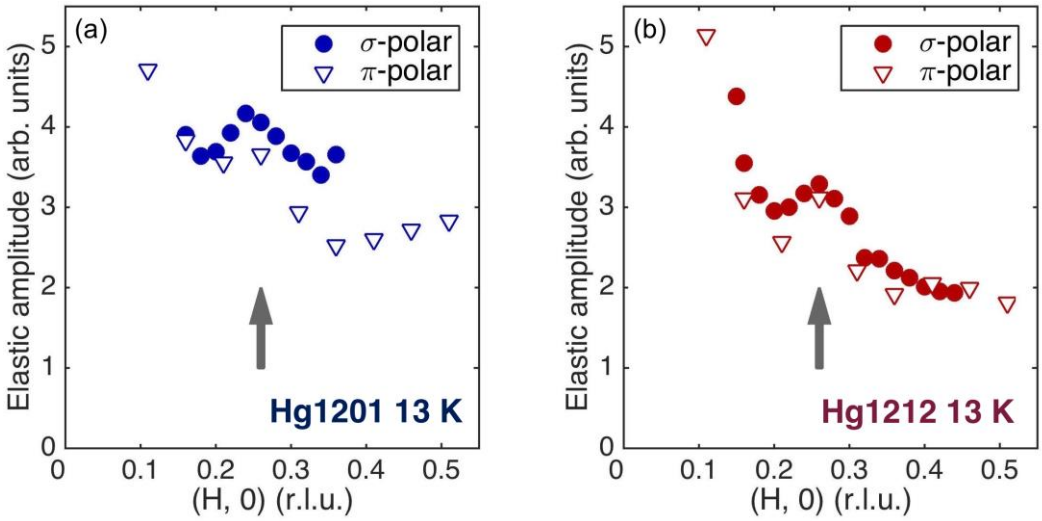

Figure S12. Signature for short-range charge order in our Hg1201 and Hg1212 samples. (a) Filled circles and empty triangles are elastic-intensity amplitudes measured with π- and σ-polarized incident x-rays, respectively, for Hg1201. The intensity maximum around $\mathbf{Q}_{//} = (0.26, 0)$ were observed with two different polarizations, indicative of charge order. (b) Same as a, but for Hg1212. Arrows indicate $H = 0.26$.

$\mathbf{Q}_{//}$ (H, K)	Hg1201				Hg1212			
	ω_{max}	ω_0	γ	ω_p	ω_{max}	ω_0	γ	ω_p
(0, 0.11)	140(19)	243(19)	243(23)		166(19)	305(19)	328(60)	
(0, 0.16)	186(19)	287(19)	257(21)	122(19)	214(19)	329(19)	285(31)	145(34)
(0, 0.21)	202(19)	317(19)	284(40)	123(47)	245(19)	361(19)	302(36)	169(32)
(0, 0.26)	226(19)	344(19)	294(40)	158(35)	264(19)	383(19)	314(37)	189(31)
(0, 0.31)	255(19)	373(21)	306(52)	206(31)	300(19)	411(19)	308(41)	268(19)
(0, 0.36)	283(19)	397(23)	306(53)	251(22)	346(19)	438(19)	282(30)	332(19)
(0, 0.41)	300(19)	415(26)	304(55)	282(19)	370(19)	454(19)	271(31)	363(19)
(0, 0.46)	316(19)	431(30)	309(63)	300(19)	384(19)	461(19)	262(26)	378(19)
(0, 0.51)	298(19)	399(19)	275(37)	289(19)	393(19)	464(19)	245(27)	393(19)
(0.07, 0.07)	133(19)	270(19)	314(40)		161(19)	306(19)	339(66)	
(0.10, 0.10)	157(19)	297(19)	322(35)		205(19)	337(19)	320(44)	
(0.13, 0.13)	163(19)	317(19)	355(68)		225(19)	363(19)	338(49)	
(0.16, 0.16)	173(20)	341(21)	384(74)		217(19)	383(22)	391(65)	
(0.19, 0.19)	164(20)	344(28)	415(98)		211(19)	398(32)	438(96)	
(0.22, 0.22)	159(20)	357(33)	448(116)		204(20)	406(38)	464(113)	
(0.25, 0.25)	157(20)	350(34)	445(119)		190(20)	413(43)	501(132)	
(0.28, 0.28)	140(20)	336(34)	449(126)		180(20)	404(45)	504(139)	
(0.31, 0.31)	125(19)	336(38)	504(136)		164(19)	380(49)	503(146)	

Table S1. Fitting parameters for the paramagnon RIXS component in Hg1201 and Hg1212. Best-fit estimates of ω_{max}, ω_0, γ and ω_p are followed by uncertainties (1 s.d.) in parentheses, all in units of meV. Values of $\mathbf{Q}_{//}$ are in units of r.l.u.

$\mathbf{Q}_{//}$ (H, K)	Increment from Hg1201 to Hg1212 (%)				
	ω_{max}	ω_p	$\omega_{p,max}$	J	$T_{c,max}$
(0, 0.11)	19(21)		**31(6)**	**30(11)**	**31**
(0, 0.16)	15(16)	19(33)			
(0, 0.21)	22(14)	38(59)			
(0, 0.26)	17(13)	20(33)			
(0, 0.31)	18(11)	30(22)			
(0, 0.36)	22(10)	32(14)			
(0, 0.41)	23(10)	29(11)			
(0, 0.46)	22(9)	26(10)			
(0, 0.51)	32(10)	36(11)			
(0.07, 0.07)	21(22)				
(0.10, 0.10)	31(19)				
(0.13, 0.13)	38(19)				
(0.16, 0.16)	26(18)				
(0.19, 0.19)	29(20)				
(0.22, 0.22)	28(21)				
(0.25, 0.25)	21(20)				
(0.28, 0.28)	29(24)				
(0.31 0.31)	32(25)				

Table S2. Percentage increase in $T_{c,max}$, J, $\omega_{p,max}$, ω_p and ω_{max} from Hg1201 to Hg1212. The values (error bars, 1 s.d.) are calculated from the data in Tables S1 and S4.

Crystal system	Tetragonal			
Compound	**$HgBa_2CuO_{4+\delta}$** [22]	**$HgBa_2CaCu_2O_{6+\delta}$** [23]	**$HgBa_2Ca_2Cu_3O_{10+\delta}$** [24]	**Disorder type**
Cu-O-Cu angle (°)	180.0	179.4	178.4	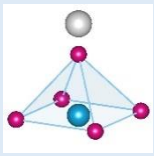
Apical Distance (Å)	2.786	2.775	2.741	
$T_{c\ max}$ (K)	97	127	135	
Space group	P4/mmm	P4/mmm	P4/mmm	
Crystal system	Orthorhombic	Tetragonal		
Compound	**$Tl_2Ba_2CuO_{6+\delta}$** [25]	**$Tl_2Ba_2CaCu_2O_{8+\delta}$** [26]	**$Tl_2Ba_2Ca_2Cu_3O_{10+\delta}$** [27]	
Cu-O-Cu angle (°)	180.0	178.4	179.4	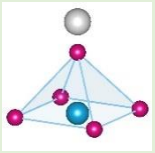
Apical Distance (Å)	2.717	2.699	2.680	
$T_{c\ max}$ (K)	93	112	127	
Space group	Fmmm	I4/mmm	I4/mmm	
Crystal system	Orthorhombic			
Compound	**$Bi_2Sr_{2-x}La_xCuO_{6+\delta}$** [28]	**$Bi_{2+x}Sr_{2-x}CaCu_2O_{8+\delta}$** [29]	**$Bi_{2+x}Sr_{2-x}Ca_2Cu_3O_{10+\delta}$** [30]	
Cu-O-Cu angle (°)	174.1	162.7/178.6	160.8 / 176.8	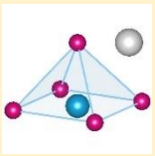
Apical Distance (Å)	2.589	2.432	2.201	
$T_{c\ max}$ (K)	38	95	111	
Space group	Cccm	Ccc2	Ccc2	
Crystal system	Orthorhombic			
Compound		**$NdBa_2Cu_3O_{6+\delta}$** [31]		
Cu-O-Cu angle (°)		163.4/165.6		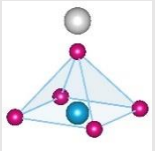
Apical Distance (Å)		2.207		
$T_{c\ max}$ (K)		95		
Space group		Pmmm		
Crystal system	Orthorhombic			
Compound		**$YBa_2Cu_3O_{6+\delta}$** [32]		
Cu-O-Cu angle (°)		165.3/166.3		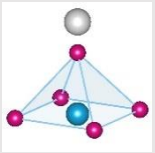
Apical Distance (Å)		2.341		
$T_{c\ max}$ (K)		93		
Space group		Pmmm		
Crystal system	Orthorhombic			
Compound		**$YBa_2Cu_4O_8$** [33]		
Cu-O-Cu angle (°)		165.2/165.7		N.A.
Apical Distance (Å)		2.294		
$T_{c\ max}$ (K)		81		
Space group		Cmmm		

Crystal system	Tetragonal /Orthorhombic	Orthorhombic		
Compound	**$La_{2-x}Sr_xCuO_4$** [34]	**$La_{2-x}Sr_xCaCu_2O_{6+\delta}$** [35]		**Disorder type**
Cu-O-Cu angle (°) Apical Distance (Å) $T_{c\ max}$ (K) Space group	176.4 / 180.0 2.414 / 2.413 39 Cmca / I4/mmm	176.0 2.310 60 I4/mmm		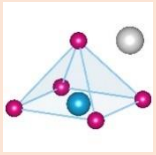
Crystal system	Tetragonal			
Compound	**$Ca_{2-x}Na_xCuO_2Cl_2$** [36]			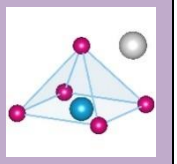
Cu-O-Cu angle (°) Apical Distance (Å) $T_{c,max}$ (K) Space group	180.0 2.753 28 I4/mmm			
Note: The structure information was obtained from the reference-linked database (ICSD data and Pearson's data).				

Table S3. Detailed structural information for different cuprates. Materials belonging to the same family, *i.e.*, as different Ruddlesden-Popper members, are classified by the same color. Cu-O-Cu angles for the triple-layer cuprates refer to the outer CuO_2 layers (the Cu-O-Cu angle of the inner CuO_2 layer is 180°) [24]. The optimally doped $La_{2-x}Sr_xCuO_4$ has two crystallographic phases: the low-temperature orthorhombic structure (Cmca) and the high-temperature tetragonal structure (I4/mmm) [34], and the corresponding Cu-O-Cu angle is 176.4° and 180.0° respectively. The space group of Bi2212 was reported to be either centrosymmetric Cccm or its non-centrosymmetric subgroup Ccc2 [29], but a very recent report [37] with higher accuracy supports Ccc2 space group. Therefore, two different Cu-O-Cu angles for Bi2212 exists due to its lower symmetry than Bi2201, and their average is smaller than that in Bi2201, *i.e.*, with further away from being a straight Cu-O-Cu bond. Bi2223 is similar to Bi2212. The illustration of chemical disorder relative to the CuO_5 pyramids or the CuO_6 octahedra is after Ref. [39].

Compound	**Reference**	$T_{c,max}$ (K)	J (meV)	$\omega_{p,max}$ (meV)
LSCO	[16]	39	157(1)	311(4)
CCOC	[17]	28	166(4)	313(5)
YBCO	[18]	93	140(2)	272(5)
Y124	[19]	81	105(2)	205(9)
NBCO	[13,19]	95	135(2)	269(6)
Tl2201	[18]	93	127(7)	247(11)
Bi2201	[8]	38	153(3)	309(15)
Bi2212	[20,21]	95	161(7)	313(11)
Bi2223	[20]	111	165(6)	324(15)
Hg1201	this work	97	135(8)	265(10)
Hg1212	this work	127	176(11)	347(8)

Table S4. $T_{c,max}$, J and $\omega_{p,max}$ of different cuprates. $\omega_{p,max}$ is the averaged propagation energy close to the zone corner ($\mathbf{Q}_{//}$ = (0.30, 0) and above). $\omega_{p,max}$ and J are determined from data and fits in Fig. S10.